Mn$^{II/III}$ and Ce$^{III/IV}$ Units Supported on an Octahedral Molecular Nanoparticle of CeO$_2$

Sayak Das Gupta, Annaliese E. Thuijs, Ethan G. Fisher, Khalil A. Abboud, and George Christou*

Read Online

ACCESS | Metrics & More | Article Recommendations | Supporting Information

ABSTRACT: The preparation of three new heterometallic clusters $[Ce_6Mn_{12}O_{17}(O_2CPh)_{26}]$ (**1**), $[Ce_{10}Mn_{14}O_{24}(O_2CPh)_{32}]$ (**2**), and $[Ce_{23}Mn_{20}O_{48}(OH)_2(tbb)_{46}(H_2O)_4](NO_3)_2$ (**3**; tbb$^-$ = 4-^{t}Bu-benzoate) is reported. They all possess unprecedented structures with a common feature being the presence of an octahedral Ce^{IV}–oxo core: a Ce$_6$ in **1**, two edge-fused Ce$_6$ giving a Ce$_{10}$ bioctahedron in **2**, or a larger Ce$_{19}$ octahedron in **3**. Complex **1** is the first Ce$_6$ cluster with a central μ_6-O^{2-}. **2** and the cation of **3** are molecular nanoparticles of CeO$_2$ (ceria) because they possess the fluorite structure of bulk ceria and are thus ultrasmall ceria nanoparticles in molecular form. The $\{Ce_{19}O_{32}\}$ octahedral subunit of the cation of **3** had been predicted from density functional theory studies to be one of the stable fragments of the CeO$_2$ lattice, but has never been previously synthesized in molecular chemistry. Around the Ce/O core of **1**–**3** is an incomplete monolayer of Mn$_n$ ions disposed as four Mn$_3$, two Mn$_7$, and four Mn$_5$ units, respectively. This represents a clear structural similarity with composite (phase-separated) CeO$_2$/MnO$_x$ mixtures where at high Ce:Mn ratios the Mn atoms segregate on the surface of CeO$_2$ phases. Variable-temperature dc and ac magnetic susceptibility studies have revealed $S = 2$, $S = \frac{1}{2}$, and $S = \frac{3}{2}$ ground states for **1**–**3**, respectively. Fitting of the 5.0–300 K dc data for **1** to a two-J model for an asymmetrical V-shaped Mn$_3$ unit with no interaction between the end Mn^{III} ions gave an excellent fit with the following values: $J_1 = 5.2(3)$ cm^{-1}, $J_2 = -7.4(3)$ cm^{-1}, and $g = 1.96(2)$.
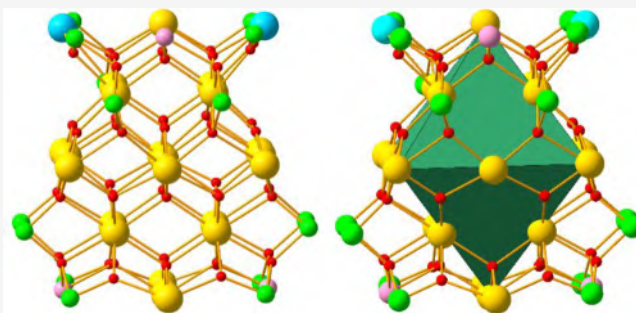
INTRODUCTION

A recent focus of our group has been to develop a molecular bottom-up approach to ultrasmall (1−10 nm) nanoparticles of important homo- and heterometallic metal oxides.[1,2] Such discrete metal–oxo clusters having the same M/O core structure as the bulk metal oxides have been named "molecular nanoparticles" (MNPs). This approach brings all of the advantages of molecular chemistry to the ultrasmall nano-particle arena, allowing for the synthesis of truly monodisperse materials identical in shape and size and offering true solubility in various solvents. Also, MNPs are crystalline in nature, allowing for structural characterization to atomic resolution by single-crystal X-ray crystallography. In the past few years, our group has reported a family of MNPs of CeO$_2$ displaying the fluorite structure (Figure 1), with Ce/O core atom counts of up to $\{Ce_{100}O_{167}\}$ and dimensions of up to 2.4 nm.[3−5] Similarly, we have also reported a family of clusters with a general formula of $[Ce_3Mn_8O_8(RCO_2)_{18}(RCO_2H)_2]$,[2,6] whose metal–oxo core is identical to the repeating unit of the AMnO$_3$ (A = lanthanide or main group metal) manganites with the perovskite structure,[7] an area of great current interest due to the important properties these mixed-metal oxides exhibit, including multiferroism.[8−10] Inspired by these successes, we have recently extended our molecular approach to seek MNPs of other important homo- and heterometallic metal oxides and

here report some recent results involving Ce/Mn chemistry unrelated to the perovskite materials but instead to composite CeO$_2$/MnO$_x$ catalysts.

Mixed CeO$_2$/MnO$_x$ materials make up an important class of heterogeneous catalysts because of their many applications in a wide range of industrial and environmental catalytic oxidation processes. Examples include oxidation of benzene[11,12] and other volatile organic compounds (VOCs) such as trichloro-ethylene, methyl *tert*-butyl ether, and chloroform[13] and catalytic oxidation of CO, which is an important part of automobile exhaust emission control.[14,15] These oxides are also used in wastewater treatment via catalytic wet oxidation of dissolved organic pollutants such as chlorinated phenols and other chloro-organics,[16,17] ammonia,[18] polyethylene glycol,[18,19] etc. They are often considered a useful alternative to noble metal catalysts, which suffer from limitations of high cost, low thermal stability, and catalyst poisoning. Studies have shown
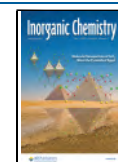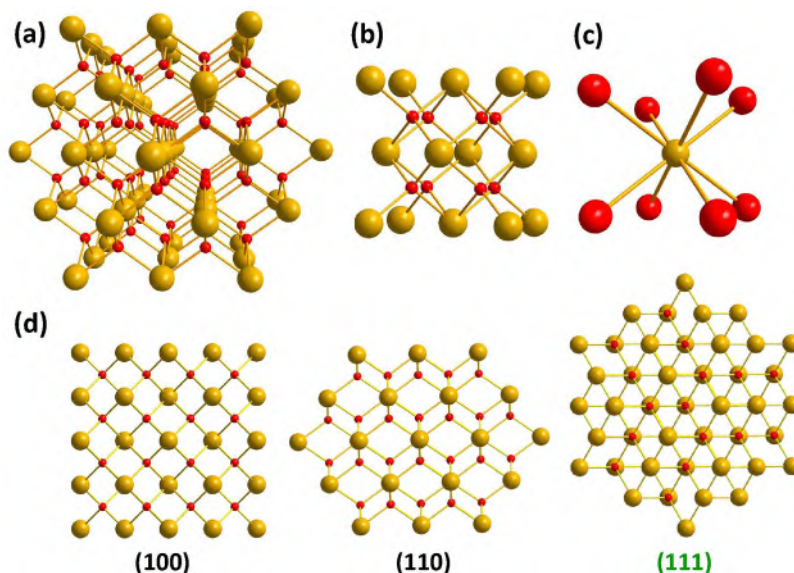
Figure 1. (a) Fluorite structure of CeO_2 emphasizing the alternating layers of Ce^{4+} and O^{2-} ions. (b) Unit cell of the CeO_2 structure. (c) One Ce^{4+} ion showing its coordination to eight oxide ions and its cubic geometry. (d) Three low-index faces of CeO_2 with the (111) color-coded according to the corresponding facets in the structural figures below: gold for Ce^{4+} and red for O.

that the catalytic activity of CeO_2/MnO_x materials can be attributed to a synergistic relationship between the Ce and Mn oxides; i.e., the catalytic activity of mixed CeO_2/MnO_x materials is higher than that of either CeO_2 or MnO_x individually.[11,17]

In Ce/Mn oxide materials with high Ce:Mn ratios, the major crystalline phase is CeO_2 with the fluorite structure, with only very small amounts of Mn dissolving in the ceria lattice to form solid solutions; the solubility of Mn^{n+} ions in ceria is reported to be only 5−10 mol %.[20] With increasing amounts of Mn, different diffraction peaks are observed from MnO_x and CeO_2, indicating the formation of composite (phase-separated) oxides.[21,22] Formation of composite oxides has been observed with as little as 15% Mn.[23] In ceria nanoparticles (CNPs) synthesized with even lower concentrations of Mn, a majority of the Mn ions segregate on the CNP surface,[24] which is attributed to the difference in ionic radii between eight-coordinate cubic Ce^{4+} (0.97 Å) and octahedral Mn (Mn^{3+}, 0.65 Å; Mn^{4+}, 0.53 Å) ions, and the lower preferred coordination number of Mn^{3+} and Mn^{4+}. This interesting segregation of Mn onto CNP surfaces and the resulting wide application of these materials in catalysis convinced us to explore whether MNPs bearing surface Mn ions could be synthesized. The general area of metal oxide nanoparticles bearing catalytic heterometals on the surface is, of course, a very topical and important one, especially supported single-atom catalysts (SACs),[25] so our investigation could provide us with important experience and expertise that could also be applied to many other systems.

The family of Ce/Mn−oxo molecular clusters has grown extensively since the first examples were reported[26,27] and now spans a range of nuclearities and Ce:Mn ratios from mainly Ce to mainly Mn, and many ratios between those extremes. Most are Ce^{IV} species, but some also contain one or more Ce^{III} ions.[28−31] This has led to interesting new magnetic molecules, including new single-molecule magnets (SMMs),[26] and molecular catalysts.[32,33] However, to date none have satisfied the requisite Ce/O core dimensions and/or structure to be seriously considered as MNPs of CeO_2 bearing surface Mn

ions. The highest nuclearity Ce/Mn clusters to date are $[Ce_{10}Mn_8O_{18}(O_2C^iPr)_{26}(H_2O)_2]$[34] and the $[Ce_5Mn_{11}O_{13}(OH)_2(O_2CPh)_{24}(NO_3)_2]^-$ anion;[35] the former has a Ce_{10} unit that is a recognizable fragment of the fluorite structure, although it is too small (<1 nm) to be considered a true MNP. We herein report three new Ce/Mn clusters: $[Ce_6Mn_{12}O_{17}(O_2CPh)_{26}]$ (**1**), $[Ce_{10}Mn_{14}O_{24}(O_2CPh)_{32}]$ (**2**), and $[Ce_{23}Mn_{20}O_{48}(OH)_2(tbb)_{46}(H_2O)_4](NO_3)_2$ (**3**). Clusters **1** and **2** are small but encouraged us that we were on the right track, and further work did indeed lead to **3**, which is both the largest Ce/Mn cluster to date and has the fluorite structure of CeO_2. It is therefore a MNP of CeO_2 and, just as importantly, has a submonolayer (incomplete shell) of Mn ions on the surface, showing clear structural similarities to the composite oxides with high Ce:Mn ratios.

■ EXPERIMENTAL SECTION

Syntheses. All manipulations were carried out under aerobic conditions using chemicals as received, unless otherwise stated. $N^nBu_4MnO_4$ was prepared as described previously.[36] **Caution!** *Appropriate care should be taken during the use of $NBu^n_4MnO_4$, and readers are referred to the detailed warning given elsewhere.*[36] Reactions were carried out in a Memmert UF 260 Plus programmable high-temperature oven to control reaction heating and cooling rates.

$[Ce_6Mn_{12}O_{17}(O_2CPh)_{26}]$ (1). Solid $PhCO_2H$ (1.00 g, 8.20 mmol) was dissolved in Ph_2O (20 mL) while being stirred at 80 °C on a hot plate, and the resulting colorless solution was treated with solid $Mn(O_2CPh)_2·2H_2O$ (0.70 g, 2.12 mmol), which resulted in a pale pink solution. Upon addition of $Ce(NO_3)_3·6H_2O$ (0.92 g, 2.12 mmol), the color of the solution changed rapidly to red. The solution was stirred at 80 °C for a further 5 min during which time solid $N^nBu_4MnO_4$ (0.19 g, 0.53 mmol) was slowly added in small portions to give a dark brown solution. This was transferred to an oven, heated to 150 °C, and maintained at this temperature for 24 h. Then it was slowly cooled over a period of 4 days to ambient temperature, which resulted in a black amorphous precipitate and a dark brown solution. When precipitation was judged to be complete, the solution was filtered and the filtrate layered with $MeNO_2$ and maintained undisturbed for 3 days during which time dark brown microcrystals slowly formed. These were collected by filtration, washed with Et_2O, redissolved in CH_2Cl_2, and layered with $MeNO_2$. X-ray quality red

Table 1. Crystal Data and Structural Refinement Parameters for Complexes 1−3

	$\mathbf{1} \cdot x(\text{solv})$	$\mathbf{2} \cdot 4\text{CHCl}_3$	$\mathbf{3} \cdot x\text{MeCN}$
formula[a]	$C_{182}H_{130}Ce_6Mn_{12}O_{69}$	$C_{224}H_{160}Ce_{10}Mn_{10}O_{88}$	$C_{506}H_{608}Ce_{23}Mn_{20}O_{152}N_2$
fw (g/mol)[a]	4920.89	6210.15	13471.57
space group	$P2_1/n$	$P2_1/c$	$I\bar{4}$
a (Å)	20.9742(8)	19.8338(4)	28.920(2)
b (Å)	30.4764(12)	31.2241(6)	28.920(2)
c (Å)	37.3100(15)	37.8585(8)	40.321(3)
α (deg)	90	90	90
β (deg)	103.4015(9)	92.0777(11)	90
γ (deg)	90	90	90
V (Å^3)	23199.8(16)	23430.1(8)	33722(5)
Z	4	4	2
T (K)	100(2)	100(2)	253(2)
λ (Å)[b]	0.71073	1.54178	0.71073
ρ_{calc} (g/cm^3)	1.798	1.958	1.315
μ (mm^{-1})	2.056	22.597	1.937
R_1[c,d]	0.0728	0.0379	0.1271
wR_2[e]	0.1646	0.0752	0.3441

[a]Excluding solvent molecules. [b]Graphite monochromator. [c]$I > 2\sigma(I)$. [d]$R_1 = 100\sum(\||F_o| - |F_c|\|)/\sum|F_o|$. [e]$wR_2 = 100\{\sum[w(F_o^2 - F_c^2)^2]/\sum[w(F_o^2)^2]\}^{1/2}$, and $w = 1/[\sigma^2(F_o^2) + (ap)^2 + bp]$, where $p = [\max(F_0^2, 0) + 2F_c^2]/3$.

plate-like crystals of $\mathbf{1} \cdot x(\text{solv})$ slowly grew from this solution over a period of 5 days. Yield: 17% based on Mn. Anal. Calcd (found) for $\mathbf{1} \cdot 6\text{H}_2\text{O}$ ($C_{182}H_{142}Ce_6Mn_{12}O_{75}$): C, 43.47 (43.15); H, 2.85 (2.72); N, 0.0 (0.0). Selected IR data (KBr, cm^{-1}): 3397 (w), 3060 (w), 1595 (s), 1540 (s), 1518 (m), 1446 (m), 1414 (s), 1359 (w), 1178 (w), 1025 (w), 840 (w), 839 (w), 715 (s), 686 (m), 686 (w), 638 (w), 608 (m), 598 (w), 539 (m), 513 (w), 491 (w), 468 (w).

$[Ce_{10}Mn_{14}O_{24}(O_2CPh)_{32}]$ (2). The precipitate from the preparation of **1** was dissolved in CHCl$_3$ and filtered, and the filtrate layered with MeCN to give X-ray quality dark-brown, block-like crystals of $\mathbf{2} \cdot 4\text{CHCl}_3$ over a period of 4 days. These were collected by filtration, washed with cold Et$_2$O, and dried under vacuum. Yield: 45% based on Mn. Anal. Calcd (found) for $\mathbf{2} \cdot 3\text{CHCl}_3$ ($C_{227}H_{163}O_{88}Cl_9Mn_{14}Ce_{10}$): C, 40.17 (40.03); H, 2.42 (2.51); N, 0.00 (0.05). Selected IR data (KBr, cm^{-1}): 3423 (w), 3062 (w), 1691 (w), 1601 (m), 1568 (m), 1545 (s), 1493 (m), 1412 (vs), 1307 (m), 1177 (m), 1156 (m), 1068 (m), 1025 (m), 1002 (w), 937 (w), 842 (w), 815 (w), 716 (s), 684 (m), 608 (m), 581 (m), 529 (m), 463 (w), 426 (w).

$[Ce_{23}Mn_{20}O_{48}(OH)_2(tbb)_{46}(H_2O)_4](NO_3)_2$ (3). 4-^{t}Bu-benzoic acid (tbbH) (0.71 g, 4.0 mmol) was dissolved in 10 mL of Ph$_2$O, followed by the addition of Mn(NO$_3$)$_2 \cdot 4\text{H}_2\text{O}$ (0.25 g, 1.0 mmol) and Ce(NO$_3$)$_3 \cdot 6\text{H}_2\text{O}$ (0.43 g, 1.0 mmol) to give a red solution. This was stirred at 80 °C for a further 5 min during which time solid N^{n}Bu$_4$MnO$_4$ (0.09 g, 0.25 mmol) was added slowly in small portions causing the color of the solution to change to very dark brown. After being stirred for an additional 1 h at 80 °C, the solution was transferred to an oven, heated to 150 °C, and maintained at this temperature for 24 h. It was then slowly cooled over 4 days, and the essentially black solution was maintained at ~40 °C on a hot plate while it was filtered. The filtrate was layered with MeCN, and the solution was left undisturbed for a week during which time deep red tetragonal crystals of $\mathbf{3} \cdot x(\text{solv})$ formed. These were collected by filtration, washed with cold MeCN, and dried under vacuum. Yield: 15% based on Ce. Anal. Calcd (found) for $\mathbf{3} \cdot 4\text{MeCN}$ ($C_{514}H_{620}Ce_{23}Mn_{20}N_6O_{152}$): C, 45.28 (45.25); H, 4.58 (4.46); N, 0.62 (0.80). Selected IR data (KBr, cm^{-1}): 3444.44 (wb), 3070.61 (w), 2963 (m), 2904 (w), 2869 (w), 1608 (m), 1584 (m), 1530 (s), 1463 (w), 1417 (s), 1362 (w), 1269 (w), 1240 (w), 1197 (m), 1155 (w), 1106 (w), 1017 (m), 856 (m), 782 (s), 711 (s), 611 (w), 581 (w), 544 (w), 486 (m), 448 (w).

X-ray Crystallography. X-ray intensity data for $\mathbf{1} \cdot x(\text{solv})$ and $\mathbf{2} \cdot 4\text{CHCl}_3$ were collected at 100 K on a Bruker DUO diffractometer, using Mo Kα radiation ($\lambda = 0.71073$ Å) for $\mathbf{1} \cdot x(\text{solv})$ and Cu Kα radiation ($\lambda = 1.54178$ Å) from an IμS power source for $\mathbf{2} \cdot 4\text{CHCl}_3$, and an APEXII CCD area detector. X-ray intensity data for $\mathbf{3} \cdot x(\text{solv})$

were collected at 253 K on a Bruker D8 VENTURE diffractometer using Mo Kα radiation ($\lambda = 0.71073$ Å) and a PHOTON III detector running the APEX3 software package of programs. Raw data frames were read with SAINT and integrated using three-dimensional profiling algorithms. The resulting data were reduced to produce *hkl* reflections and their intensities and estimated standard deviations. The data were corrected for Lorentz and polarization effects, and numerical absorption corrections were applied on the basis of indexed and measured facets. Structural refinements were carried out using full-matrix least-squares refinements by minimizing the wR_2 function using F^2 values. R_1 is calculated to provide a reference to the conventional R value, but its function is not minimized. Crystal data and structural refinement parameters are listed in Table 1.

For $\mathbf{1} \cdot x(\text{solv})$ and $\mathbf{2} \cdot 4\text{CHCl}_3$, the structures were determined and refined in *SHELXTL2014*.[37] Non-H atoms were refined with anisotropic thermal parameters, and all H atoms were placed in calculated, idealized positions and refined as riding on their parent atoms. The asymmetric unit of $\mathbf{1} \cdot x(\text{solv})$ consists of the Ce$_6$Mn$_{12}$ cluster and an estimated 10 MeNO$_2$ and 8 CH$_2$Cl$_2$ solvent molecules. Most of these were too disordered to be modeled properly; thus, SQUEEZE,[38] a part of the PLATON package of crystallographic software, was used to calculate the solvent disorder area and remove its contribution to the overall intensity data. There are 13 disordered benzoate Ph rings, and each was refined in two sites with their site occupation factors fixed in the final refinement model. Most of the Ph rings were idealized by "AFIX 66" and EADP in the final refinement. In the final cycle of refinement, 53287 reflections [of which 32212 are observed with $I > 2\sigma(I)$] were used to refine 2022 parameters and the resulting R_1, wR_2, and S (goodness of fit) were 7.28%, 16.46%, and 1.047, respectively.

The asymmetric unit of $\mathbf{2} \cdot 4\text{CHCl}_3$ consists of the Ce$_{10}$Mn$_{14}$ cluster and four CHCl$_3$ solvent molecules. The latter were too disordered to be modeled properly; thus, SQUEEZE was again used. In the final cycle of refinement, 40675 reflections [of which 26856 are observed with $I > 2\sigma(I)$] were used to refine 3025 parameters and the resulting R_1, wR_2, and S (goodness of fit) were 3.79%, 7.52%, and 0.919, respectively.

For $\mathbf{3} \cdot x(\text{solv})$, the structures were determined and refined in *SHELXTL2014*[37] and *SHELXL2018*.[39] Intrinsic phasing structure solution provided the heavy atom positions in space group $I\bar{4}$ and some of the coordinated O atoms. The crystals provided very low diffraction and very low-resolution data regardless of what experimental parameters were employed. Diffraction frames looked like patches of diffuse scattering with occasional intensity spots, while at low 2θ values, the reflections were very intense. Variations of the

crystal size, exposure time, and data collection temperature were explored to optimize the measured intensities and achieve the highest possible resolution. The final refined model necessitated using a resolution of 0.94 Å or a high 2θ of 45°. Beyond this limit, reflections were not observed. The initial electron density map provided the Ce, Mn, O, and OCO C atoms. Further difference Fourier maps provided electron density peaks from some Ph C atoms, but subsequent maps did not provide further information about the rest of the tbb⁻ ligand atoms. Starting with three C positions of any Ph ring, SHELX allowed the rest of the ring atoms to be placed in idealized positions (using command AFIX 66), as well as the ᵗBu C atoms, which were not observed in difference Fourier maps. SHELX commands AFIX 66, SADI, FLAT, and SAME were used to constrain the ligands to maintain idealized geometries. In addition, solvent molecules could not be reliably identified, and thus, SQUEEZE was again used, which revealed a solvent accessible area of 9504 Å³ and 2959 total electrons in the unit cell. Finally, only the Ce, Mn, and O atoms were refined anisotropically, while isotropic displacement parameters for the C atoms were fixed at 0.1. In the final cycle of refinement, 22039 reflections [of which 14967 are observed with $I > 2\sigma(I)$] were used to refine 677 parameters and the resulting R_1, wR_2, and S (goodness of fit) were 12.71%, 34.41%, and 2.550, respectively.

Other Studies. Infrared spectra were recorded in the solid state (KBr pellets) on a Nicolet Nexus 670 FTIR spectrometer in the range of 400−4000 cm⁻¹. Elemental analyses (C, H, N) were carried out at Atlantic Microlab, Inc. Direct current (dc) and alternating current (ac) magnetic susceptibility measurements were performed on vacuum-dried polycrystalline solids, embedded in eicosane to prevent torquing, with a Quantum Design MPMS-XL SQUID magnetometer capable of operating with applied dc fields of ≤7 T in the range of 1.8−400 K. dc studies were carried out in the range of 5.0−300.0 K in a 0.1 T (1000 G) magnetic field, and ac studies in the range of 1.8−15.0 K in an ac field of 3.5 G and oscillation frequencies of ≤1500 Hz. The program PHI[40] was used for fitting the dc susceptibility data.

RESULTS AND DISCUSSION

Syntheses. The complexes in this work were all prepared from a hybrid of two procedures we have frequently used in homometallic Mn and Ce chemistry. For the former, we often use a comproportionation reaction between a Mn^{2+} salt and MnO_4^- in the presence of a carboxylic acid. On the contrary, in the latter area we have prepared a family of molecular nanoparticles of CeO_2 from the hydrolysis reactions of Ce^{3+} and/or Ce^{4+} salts with carboxylic acids.[1,4] Thus, in this work we have employed a comproportionation reaction between a Mn^{2+} salt and MnO_4^- in the presence of $Ce(NO_3)_3$ and RCO_2H in a 4:1:4:16 molar ratio in diphenyl ether at 150 °C for 24 h. Slow cooling of the R = Ph reaction with $Mn(O_2CPh)_2$ to room temperature over 4 days led to the formation of a dark-colored solution and a black precipitate, from which were obtained $1 \cdot x(solv)$ and $2 \cdot 4CHCl_3$, respectively, after filtration and subsequent workup. Use of tbbH and $Mn(NO_3)_2$ instead of $PhCO_2H$ and $Mn(O_2CPh)_2$ in the same reaction scheme gave no precipitate on cooling and led to subsequent isolation of $3 \cdot x(solv)$. Complexes **1**−**3** are in the $Ce^{IV}_6Mn^{III}_{12}$, $Ce^{IV}_{10}Mn^{III}_{12}Mn^{II}_2$, and $Ce^{IV}_{21}Ce^{III}_2Mn^{III}_{16}Mn^{II}_4$ oxidation states, respectively.

Description of Structures. Core structural figures with all metal ions labeled are provided as Figures S1−S3. Metal oxidation states and the absence of protons on the core oxides were confirmed by Ce/Mn and O bond valence sum (BVS) calculations, respectively (Tables S1−S3).[41]

Complex **1** has no crystallographic symmetry but has virtual D_2 symmetry if the Ph ring orientations are ignored (Figure 2a). Its $\{Ce^{IV}_6Mn^{III}_{12}O_{17}\}^{26+}$ core comprises a Ce_6 octahedron bridged at the center by a rare μ_6-O^{2-} ion (O1) and on each of
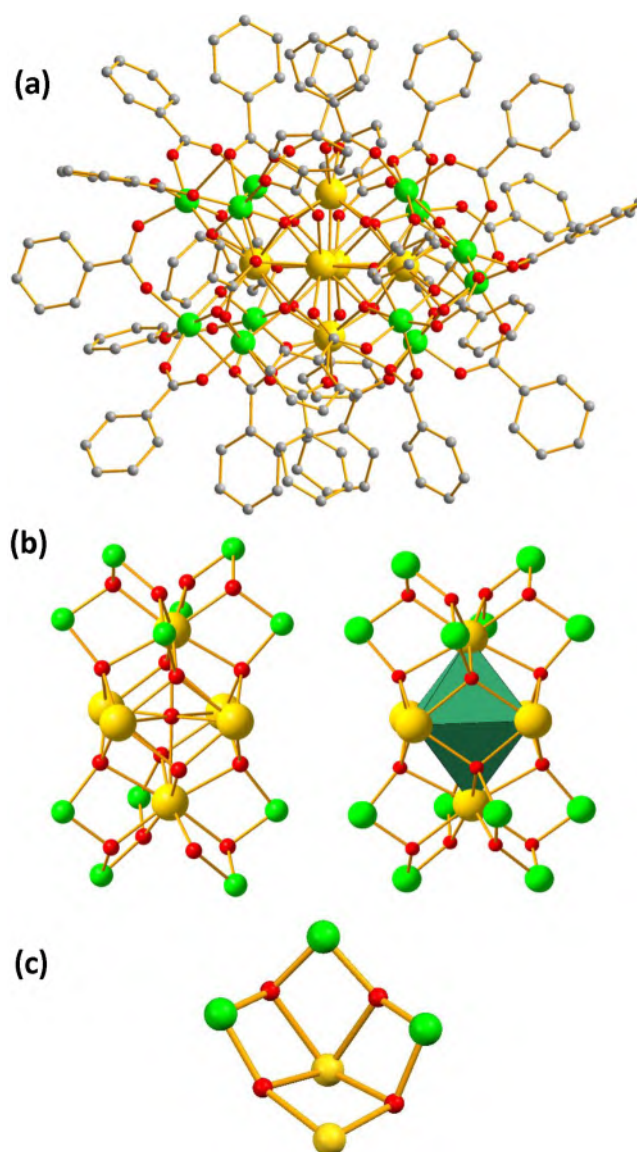

Figure 2. (a) Structure of complete **1**, with H atoms omitted for the sake of clarity. (b) Its core from a different viewpoint emphasizing the μ_6-O^{2-} and the facets. (c) V-Shaped $\{Mn_3O_2\}$ unit and its means of attachment to the Ce/O surface, emphasizing the bridging of all Mn ions to core Ce^{IV} ions. Color code: gold for Ce^{IV}, green for Mn^{III}, red for O, and gray for C.

the eight Ce_3 faces by a μ_3-O^{2-} ion that then becomes μ_4 by attachment to an outer Mn^{III} (Figure 2b). The core is surrounded by 12 Mn^{III} ions, occurring as four V-shaped $\{Mn_3(\mu$-$O)_2\}$ units whose oxides become μ_3 by bonding to the same Ce ion (Figure 2c). Eight of these Mn, two in each Mn_2 unit, are clearly near-octahedral with a Jahn−Teller (JT) axial elongation and resulting long Mn−O bonds in the range of 2.107(5)−2.310(6) Å. However, the other four (Mn3, Mn6, Mn9, and Mn12), the central Mn ions in the Mn_3 units, could be described as either severely JT-distorted octahedral with one elongated Mn−O bond in the range of 2.498(6)− 2.604(6) Å or square pyramidal with a long sixth Mn··O contact, the latter O being from a multiply bridging $PhCO_2^-$ ligand, which can be described as μ_4- or μ_3-bridging, respectively. We feel the distorted octahedral description and a μ_4-benzoate to be more accurate, and this point will be

discussed further in the magnetic studies (vide infra). In addition to these ligands, the peripheral ligation includes 18 common *syn,syn* $\eta^1:\eta^1:\mu$-benzoates (10 bridging Mn_2 pairs and eight bridging CeMn pairs) and four $\eta^2:\eta^1:\mu_3$-benzoates bridging $CeMn_2$ units (Scheme 1).

Scheme 1. Carboxylate Binding Modes in 1−3
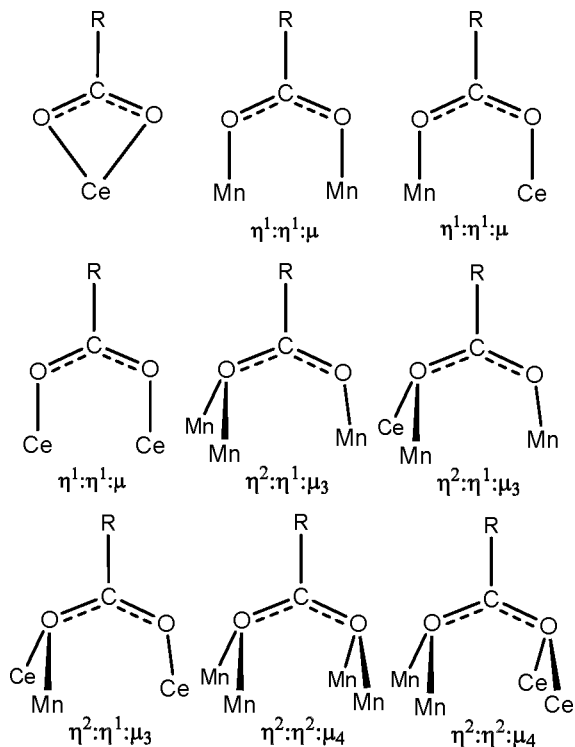
The Ce_6−oxo octahedral unit is the smallest reasonable repeating unit of the fluorite lattice and has been previously isolated as a discrete Ce_6−oxo homometallic cluster[42,43] as well as in Ce/Mn−oxo heterometallic clusters.[30,31] In the former case, the faces are typically μ_3-bridged by a mixture of O^{2-} and OH^- ions, but exceptions exist. In heterometallic clusters, they tend to be all O^{2-}, some of them binding to external Mn ions as seen in **1**. Nevertheless, **1** is unique in having all of its O^{2-} ions bound to Mn, and in addition, this is the first example of a central μ_6-O^{2-} in a Ce−oxo or Ce/Mn−oxo cluster, to the best of our knowledge, although there is precedent for its occurrence in other metal chemistry.[44]

Complex **2** has no crystallographic symmetry but has virtual C_i symmetry if the Ph ring orientations are ignored (Figure 3a). It has a structure related to **1** in that its $[Ce^{IV}_{10}Mn^{II}_2Mn^{III}_{12}O_{24}]^{32+}$ core consists of two Ce_6 octahedra joined together into an edge-fused Ce_{10} bioctahedron, eight of whose μ_3-O^{2-} ions then become μ_4 by attachment to an outer Mn^{II} or Mn^{III} leaving four μ_3-O^{2-} ions bridging Ce_3 faces (Figure 3b). There are two additional μ_4-O^{2-} ions bridging the two octahedra on either side of the shared edge. The 14 Mn atoms separate into two $\{Mn^{III}_6Mn^{II}(\mu_3$-$O)_5\}$ units attached to either side of the Ce_{10} bioctahedron to give a $Mn_7Ce_{10}Mn_7$ sandwich-like arrangement (Figure 3b,c). The Mn^{II} (Mn4, Mn11) and two of the Mn^{III} ions are five-coordinate square pyramidal, and the rest are near-octahedral and exhibit JT axial elongations. The peripheral ligation is completed by 22 $\eta^1:\eta^1:\mu$-benzoates (10 bridging Mn_2 pairs and 12 bridging CeMn pairs), six $\eta^2:\eta^1:\mu_3$-benzoates (two each bridging the
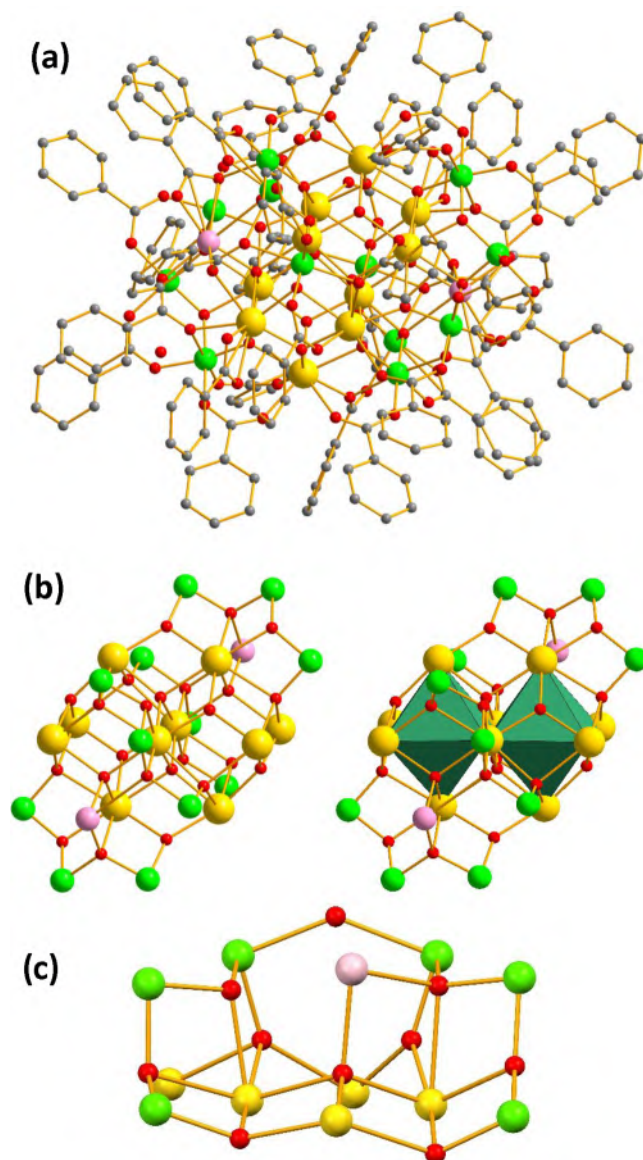

Figure 3. (a) Complete structure of complex **2**, with H atoms omitted for the sake of clarity. (b) Metal−oxo core from a different viewpoint. (c) $\{Mn_7O_5\}$ unit and its means of attachment to the Ce/O surface, emphasizing the bridging of all Mn ions to core Ce^{IV} ions. Color code: yellow for Ce^{IV}, green for Mn^{III}, pink for Mn^{II}, red for O, and gray for C.

Mn_3, Mn_2Ce, and $MnCe_2$ units), two true (and rare) $\eta^2:\eta^2:\mu_4$-benzoates, and two benzoates chelating to separate Ce ions (Scheme 1).

The Ce_{10} bioctahedral unit is again a recognizable small unit of the fluorite lattice and has never been previously reported in a discrete homometallic cluster, the few known Ce_{10} clusters having very different structures.[45,46] However, it is of course a recognizable subunit of higher-nuclearity Ce_x clusters, and it has also been seen in the heterometallic $[Ce_{10}Mn_8O_{18}(O_2CR)_{26}(H_2O)_2]$ cluster.[34]

The cation of **3** is the largest Ce/Mn cluster to date (Figure 4a). It has crystallographically imposed S_4 symmetry, the asymmetric unit containing one-fourth of the molecule. It is a continuation of the structural trend seen in **1** and **2** but now with a much larger Ce_{23}−oxo core clearly exhibiting the fluorite structure of bulk CeO_2 and with 16 Mn^{III} and 4 Mn^{II}
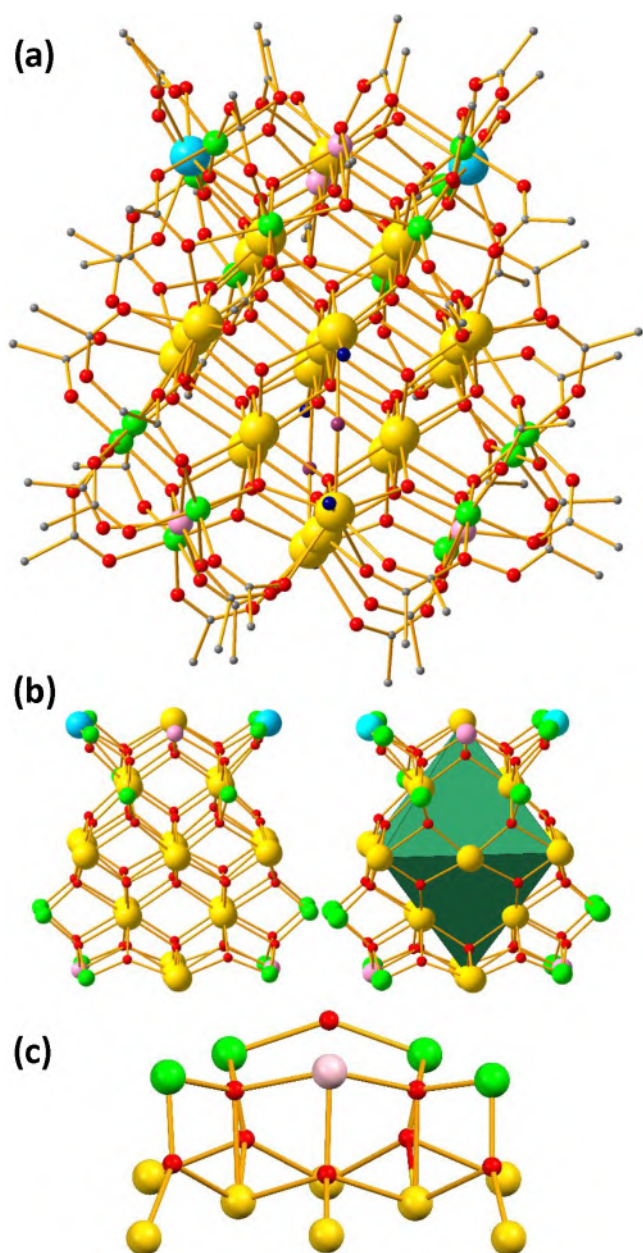
Figure 4. (a) Structure of **3**, with only Ph *ipso* C atoms shown and all H atoms omitted for the sake of clarity. (b) Metal−oxo core from a slightly different viewpoint. (c) $\{Mn_5O_2\}$ unit and its means of attachment to the Ce/O surface, emphasizing the bridging of all Mn ions to core Ce^{IV} ions. Color code: gold for Ce^{IV}, sky blue for Ce^{III}, green for Mn^{III}, pink for Mn^{II}, red for O, purple for OH^-, and deep blue for H_2O.

ions surrounding it (Figure 4b,c). However, the high crystallographic symmetry of the metal−oxo core, resulting disorder in the Ce^{III} positions, and a μ-HO^- versus μ-RCO_2^- disorder at four positions between Ce4 and Ce5 as well as disorder among the tbb^- ligands made it difficult to identify some details with a high level of precision. Nevertheless, on the basis of Ce and Mn BVS values and charge balance considerations, we concluded that there are 21 Ce^{IV} ions and two Ce^{III} ions, the latter disordered among the four symmetry-related Ce4 ions on the surface.

The core of the complex is best described as a $\{Ce^{IV}_{19}O_{32}\}$ octahedron comprising five Ce layers in a 1:4:9:4:1 A:B:C:B:A

pattern, to the surface of which are attached four more Ce atoms (Ce4) and four $\{Mn_5O_4\}$ units to give the complete $[Ce^{IV}_{21}Ce^{III}_2Mn^{III}_{16}Mn^{II}_4O_{48}]^{50+}$ metal−oxo unit (Figure 4b). The four Ce4 atoms and four Mn_5 units both form concentric tetrahedra about the $\{Ce_{19}O_{32}\}$ octahedron, and the whole core can thus be described as a supertetrahedron. This is surrounded by an organic ligand shell of 46 tbb^- anions, two OH^- anions, and four terminal H_2O ligands, leading to an overall charge of +2. The elemental analysis supports the presence of two NO_3^- counterions in the dried material, but they could not be crystallographically identified in the disordered solvent. The peripheral ligation of tbb^- ligands exhibits three binding modes. Twenty-four are $\eta^1:\eta^1:\mu$ with 8 and 16 bridging Mn_2 and CeMn pairs, respectively; 16 are $\eta^1:\eta^2:\mu_3$ with 4 and 12 bridging Mn_3 and $CeMn_2$ units, respectively; four are $\eta^2:\eta^2:\mu_4$ across a Ce_2Mn_2 unit, and two are $\eta^2:\eta^1:\mu$ bridging a Ce_2 pair but disordered with the two bridging OH^- ions and four terminal H_2O ligands among four symmetry-equivalent positions, as shown in Figure S4.

Complex 3 as a Molecular Nanoparticle. Complexes **1** and **2** are too small (longest core dimension of <1 nm) to be reasonably considered MNPs of CeO_2. Nevertheless, they provide interesting points of comparison with the cation of **3**, which is large enough to clearly exhibit the fluorite structure and a $\{Ce_{19}O_{32}\}$ octahedral core with dimensions of 1.1 nm × 1.1 nm × 1.1 nm. It is thus in the size regime of an ultrasmall nanoparticle of CeO_2, and the four additional Ce^{III}/Ce^{IV} metal atoms attached on the surface can be considered the growth points of the next shell of Ce atoms, but terminated by the incorporation of the Mn ions.

Interestingly, the $\{Ce_{19}O_{32}\}$ octahedral unit is identical to one of the members of the family of octahedron-shaped nanoparticles of CeO_2 with a general formula of $Ce_xO_{2(x-n)}$ (n = 2, 3, 4, etc.), where x is given by eq 1, which were predicted from density functional theory studies to be the most stable fragments of CeO_2.[47]

$$x = \frac{n(2n^2 + 1)}{3} \tag{1}$$

The $\{Ce_6O_8\}$ and $\{Ce_{19}O_{32}\}$ octahedra of **1** and **3**, respectively, correspond to the n = 2 and 3 members, and the next members, n = 4 and 5, would be $\{Ce_{44}O_{80}\}$ and $\{Ce_{85}O_{160}\}$ with 1:4:9:16:9:4:1 and 1:4:9:16:25:16:9:4:1 layers and dimensions of ~1.5 and ~2.0 nm, respectively (Figure 5). These are both smaller than the $\{Ce_{100}O_{167}\}$ MNP that we reported recently[5] and should be attainable, and we look forward to possibly obtaining one or both of them as MNPs as this work progresses. In fact, a MNP related to the $\{Ce_{44}O_{80}\}$ octahedron has already been obtained, $[Ce_{38}O_{54}(OH)_8(O_2CEt)_{36}(py)_8]$,[1] which has a $\{Ce_{38}O_{62}\}$ core where the six Ce ions at the six points of the $\{Ce_{44}O_{80}\}$ octahedron have been lost together with three of the four O^{2-} ions attached to each one, leaving a "truncated octahedron" with the remaining O^{2-} at each point becoming a μ_4-OH^-; it thus has a 4:9:12:9:4 layer structure. This Ce_{38} MNP is also relevant to CNPs, because high-resolution transmission electron microscopy studies have shown that larger CNPs (>10 nm or so) are often octahedral in shape, whereas CNPs in the 3−10 nm range are truncated-octahedral.[48] Two additional reports of Ce_{38} clusters have recently appeared from other groups,[49] as well as a Ce_{70} wheel-like cluster.[50] We thus assign the perfect octahedral core of **3** to the stabilizing
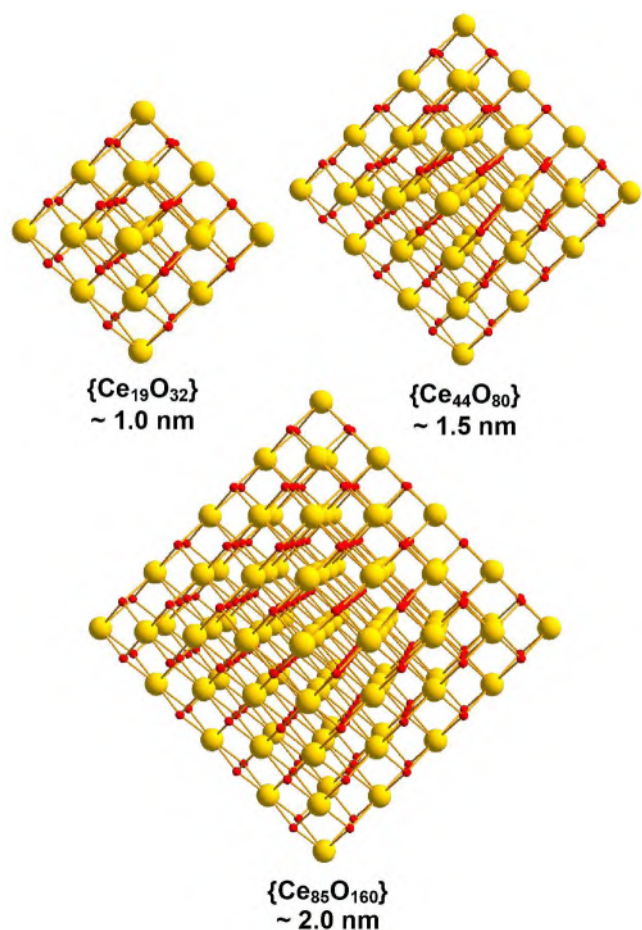
Figure 5. Comparison of the size and atom count of the $\{Ce_{19}O_{32}\}$ core of **3** with those for the next two sizes of Ce_x octahedra calculated from eq 1. Color code: gold for Ce^{IV} and red for O.

effect of the four additional Ce and Mn_5 units on the surface, and obtaining the larger $\{Ce_{44}O_{80}\}$ and $\{Ce_{85}O_{160}\}$ in MNPs as perfect octahedra may thus also require heterometallic Ce/Mn chemistry. Also welcome, however, would be the truncated octahedron in homometallic $\{Ce_{79}O_{142}\}$ with a 4:9:16:21:16:9:4 layer structure.

Among the previously reported MNPs of CeO_2 we observed all three of the low-index surface facets, with (111) > (100) > (110) (Figure 1) being the order of occurrence, the (110) being seen only in the larger Ce_{40} and Ce_{100} clusters.[1,5] This parallels the recognized thermodynamic stability in CNPs, with the (111) facets being the most stable and the (100) and (110) facets being the sites of high catalytic activity.[51] The octahedral topology in **1–3** corresponds to only (111) facets, most apparent in the larger $\{Ce_{19}O_{32}\}$ core of **3** with its large (111) facets each comprising six Ce ions in four edge-fused triangles. The $\{Ce_6\}$ and $\{Ce_{10}\}$ units in **1** and **2** are composed of eight and 16 (111) facets, respectively, but all consisting of single Ce_3 triangles.

Complex 3 as a Molecular Model of a Composite Oxide. As mentioned above, all of the Mn ions of **1–3** are attached directly to the Ce/O cores by one or more monatomic O atoms (Figure 2), giving a submonolayer of Mn ions. In particular for **3** with its large $\{Ce_{19}O_{32}\}$ core, the analogy is apparent with the segregation of Mn at low doping levels onto the surface of the CeO_2 catalysts leading to enhanced catalytic activity. Thus, **3** represents a molecular

analogue of 3d metal catalysts on an ultrasmall metal oxide nanoparticle support. At higher Mn loadings, one can readily envisage growth of the Mn/O units into multilayers giving molecular analogues of the phase-separated MnO_x/CeO_2 composites, but we have not come across such molecular species to date. We also note that **3** suggests that it may be possible to attain clusters with the Mn replaced with other 3d or 4d/5d metals.

Direct Current (dc) Magnetic Susceptibility Studies. Variable-temperature dc magnetic susceptibility (χ_M) data were collected on crushed vacuum-dried microcrystalline samples of $\mathbf{1}\cdot6H_2O$, $\mathbf{2}\cdot3CHCl_3$, and $\mathbf{3}\cdot4MeCN$ in the range of 5.0–300 K in a 0.1 T (1 kG) applied dc field and are plotted as $\chi_M T$ versus T (Figure 6). Because Ce^{IV} is diamagnetic, all of the paramagnetism arises from Mn^{II}, Mn^{III}, and Ce^{III} ions.
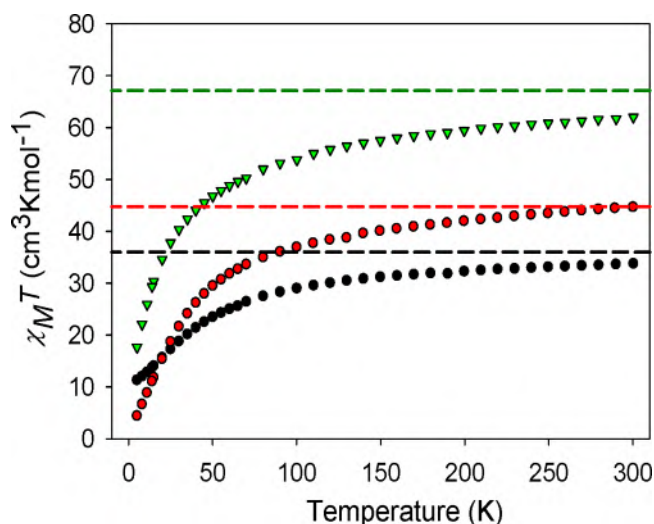

Figure 6. Plots of $\chi_M T$ vs T for $\mathbf{1}\cdot6H_2O$ (●), $\mathbf{2}\cdot3CHCl_3$ (red circles), and $\mathbf{3}\cdot4MeCN$ (green triangles). The dashed lines show the calculated $\chi_M T$ with $g = 2.0$ if all metal ions are non-interacting.

For $\mathbf{1}\cdot6H_2O$, $\chi_M T$ gradually decreases from 33.78 cm^3 K mol^{-1} at 300 K to 27.48 cm^3 K mol^{-1} at 80 K, followed by a steeper decrease to 11.31 cm^3 K mol^{-1} at 5.0 K. The 300 K value is lower than the spin-only ($g = 2.0$) $\chi_M T$ for 12 non-interacting Mn^{III} ions (36.00 cm^3 K mol^{-1}), indicating dominant antiferromagnetic (**AF**) interactions within the cluster. Similar profiles are observed for $\mathbf{2}\cdot3CHCl_3$ and $\mathbf{3}\cdot4MeCN$. For $\mathbf{2}\cdot3CHCl_3$, $\chi_M T$ is 44.75 cm^3 K mol^{-1} at 300 K, essentially that for 12 Mn^{III} and two Mn^{II} non-interacting ions (44.68 cm^3 K mol^{-1}), and decreases with T to 4.41 cm^3 K mol^{-1} at 5.0 K. For $\mathbf{3}\cdot4MeCN$, $\chi_M T$ is 62.00 cm^3 K mol^{-1} at 300 K, less than the calculated value of 67.12 cm^3 K mol^{-1} for 16 Mn^{III} and 4 Mn^{II} non-interacting ions (65.5 cm^3 K mol^{-1}; $g = 2.0$) plus 1.62 cm^3 K mol^{-1} for two Ce^{III} ions ($S = {}^1/_2$, $L = 3$, $J = {}^5/_2$), and decreases with T to 53.14 cm^3 K mol^{-1} at 90.0 K and then to 17.64 cm^3 K mol^{-1} at 5.0 K. Thus, complexes **1–3** all exhibit mainly or wholly **AF** interactions within their Mn_x units.

Because the 12 Mn^{III} ions in $\mathbf{1}\cdot6H_2O$ occur as four Mn_3 units separated by a minimum of four bonds through diamagnetic Ce^{IV} ions, it is reasonable to assume any inter-Mn_3 interactions would be very weak and affect only the $\chi_M T$ versus T data at the very lowest temperatures. We thus fit the data as arising from four independent and identical Mn_3 units, using the two-J

model shown as the inset in Figure 7. This model reflects the fact that the V-shaped Mn_3 unit is clearly too asymmetric to
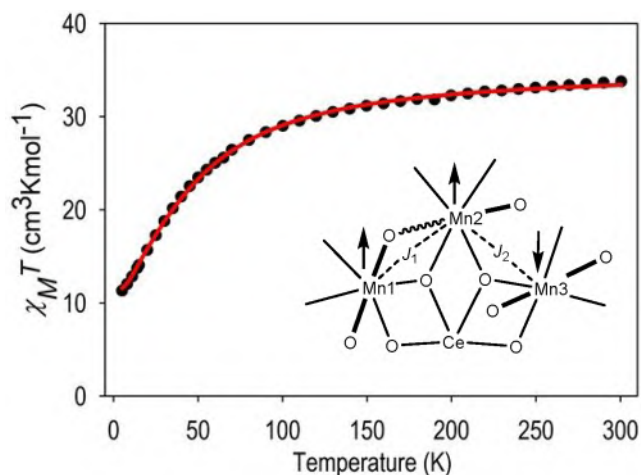

Figure 7. Plot of $\chi_M T$ vs T for **1**·$6H_2O$ and its fit (solid red line) using PHI to the two-J model shown as the inset. The Mn numbering is arbitrary and does not correspond to the atom labels in the structure. The thicker bonds indicate the location of the Mn^{III} JT elongation axes. The long Mn··O contact [2.498(6)−2.604(6) Å] is shown as a squiggle. See the text for the fit parameters.

warrant a one-J (i.e., $J_1 = J_2$) model and also again assumes that the four-bond interaction pathway between Mn1 and Mn3, this time intra-Mn_3, will lead to an exchange interaction (J_3) of insignificant magnitude. The spin Hamiltonian for the two-J model for each Mn_3 is given by eq 2

$$\mathcal{H} = -2J_1\hat{S}_1\hat{S}_2 - 2J_2\hat{S}_2\hat{S}_3 \tag{2}$$

where S_i is the spin of metal ion Mn_i and $S_1 = S_2 = S_3 = 2$. The fit using PHI gave $J_1 = 5.2(3)$ cm^{-1}, $J_2 = -7.4(3)$ cm^{-1}, and $g = 1.96(2)$, with temperature-independent paramagnetism (TIP) kept constant at 300×10^{-6} cm^3 mol^{-1}. This combination of ferromagnetic (**F**) J_1 and **AF** J_2 gives the spin vector alignments in Figure 7 (inset) with a resultant $S = 2$ ground state for each Mn_3 unit. This should give a total spin-only ($g = 2.0$) $\chi_M T$ of 12.0 cm^3 K mol^{-1} for four Mn_3 units, or slightly less for $g < 2$ as expected for Mn^{III}, which is consistent with the 5.0 K value in Figure 7.

The larger Mn_7 and Mn_5 units of **2** and **3**, respectively, and the resulting greater number of inequivalent J values they contain discouraged us for overparametrization reasons from attempting to fit the data. We instead just targeted identifying the ground state S value, but because they both also contain Mn^{II} ions, which are known to give very weak exchange couplings and thus a high density of low-lying excited states, we turned to the use of ac susceptibility to preclude complications from the presence of the dc field.

Alternating Current (ac) Magnetic Susceptibility Studies. ac susceptibility data were collected on crushed vacuum-dried microcrystalline samples of **1**·$6H_2O$, **2**·$3CHCl_3$, and **3**·$4MeCN$ in the range of 1.8−15.0 K in a 3.5 G ac field with a 1000 Hz oscillation frequency and in a zero dc field. The obtained in-phase ac susceptibilities (χ'_M) are plotted as $\chi'_M T$ versus T in Figure 8.

For **1**·$6H_2O$, $\chi'_M T$ has almost reached a plateau by 5.0 K, and the data from >3 K extrapolate to ~11.2 cm^3 K mol^{-1} at 0 K (Figure 8a). This is the total $\chi'_M T$ for four Mn_3 units and

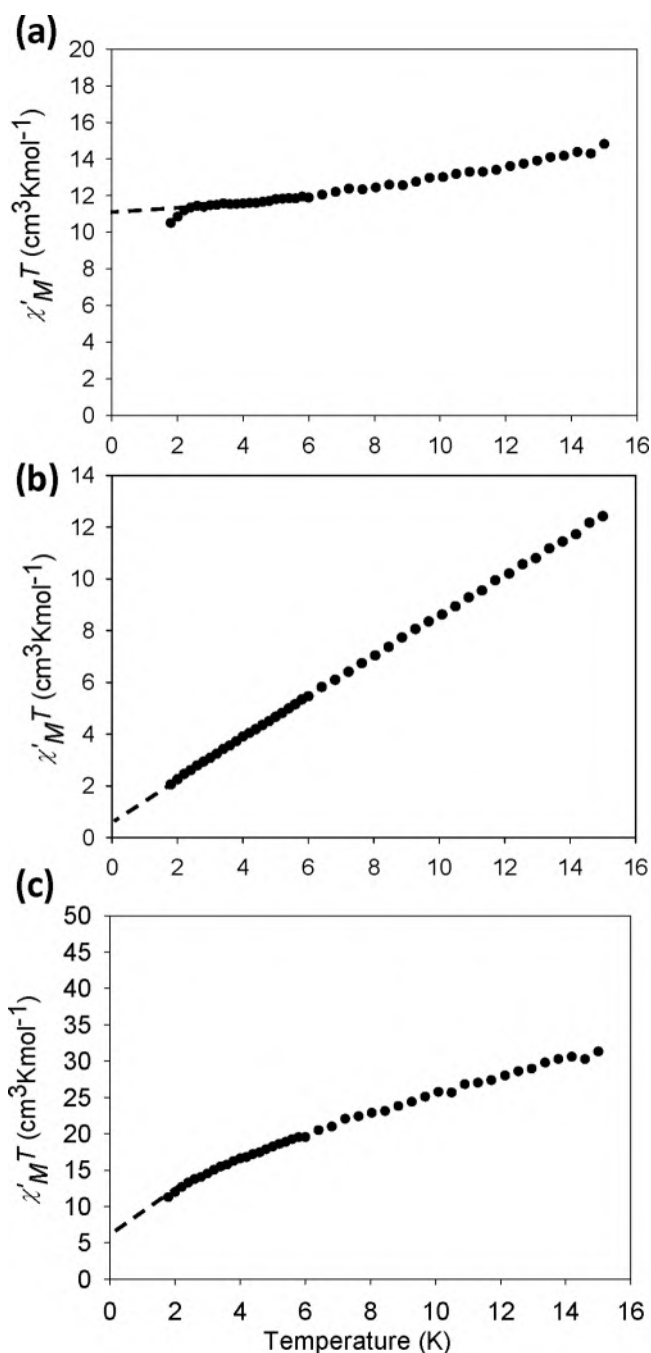**Figure 8.** ac in-phase $\chi'_M T$ vs T data for (a) **1**·$6H_2O$, (b) **2**·$3CHCl_3$, and (c) **3**·$4MeCN$. See the text for the estimated ground states.

thus corresponds to ~2.8 cm^3 K mol^{-1} per Mn_3, as expected for an $S = 2$ system with $g < 2.0$ slightly. It thus independently confirms the conclusion from the dc study that the ground state of each Mn_3 unit is $S = 2$ and that they are essentially non-interacting. In fact, the small decrease below 3 K that was ignored in the extrapolation is likely due to any inter-Mn_3 interaction (and/or zero-field splitting within the ground state).

For **2**·$3CHCl_3$, $\chi'_M T$ decreases rapidly with a decrease in temperature from 15 K, consistent with depopulation of low-lying excited states with a spin greater than the ground state, as expected from the presence of Mn^{II} and dominant **AF** interactions, respectively (Figure 8b). Extrapolation to 0 K

gives a value of ~ 0.7 cm^3 K mol^{-1} as expected for two non-interacting Mn$_7$ units each with an $S = {}^1/_2$ ground state and $g <$ 2 slightly. For **3**·4MeCN, $\chi'_M T$ again decreases rapidly with temperature (Figure 8c) and extrapolates to the range of 6−7 cm^3 K mol^{-1} at 0 K, as expected for four non-interacting Mn$_5$ units each with an $S = {}^3/_2$ ground state and $g <$ 2 slightly; the spin-only ($g = 2$) values for four $S = {}^1/_2$, ${}^3/_2$, and ${}^5/_2$ units are 1.5, 7.5, and 17.5 cm^3 K mol^{-1}, respectively.

Rationalization of the Exchange Coupling in 1. Consideration of the structural features around each Mn$_3$ unit of **1**·6H$_2$O, as shown in the inset of Figure 7, leads to a reasonable rationalization of the **F** and **AF** nature of J_1 and J_2, respectively. In the discussion below, we employ the arbitrary Mn labeling of Figure 7 (inset) for the sake of convenience, and we consider the central Mn of each Mn$_3$ unit as highly JT-elongated octahedral with one JT Mn−O bond [2.498(6)−2.604(6) Å] being significantly longer than the other [2.063(6)−2.086(6) Å]. That the former is structurally significant is shown by the fact that it makes the adjacent Mn1−O^{2-}−Mn2 angle [108.2(3)−109.1(3)°] significantly more acute than the Mn2−O^{2-}−Mn3 angle [128.8(3)−130.4(3)°]. Under this description, the JT axes on Mn1 and Mn2 are meeting at the bridging carboxylate atom with even more acute angles of 78.0(3)−79.3(3)°. Because the JT axes define the local z-axis at each Mn^{III}, the situation that results is that the two d$_{z^2}$ σ-symmetry magnetic orbitals are meeting at the bridging carboxylate O atom with very acute angles that should favor a net **F** J_1 interaction, as determined experimentally. In contrast, the JT axis at Mn3 is not meeting that of Mn2, and the interaction should be dominated by dπ−dπ overlaps across the larger Mn2−O^{2-}−Mn3 angles suggesting an **AF** J_2 interaction, as determined experimentally. For the larger Mn$_7$ and Mn$_5$ units of **2**·3CHCl$_3$ and **3**·4MeCN, which contain many more pairwise interactions, we cannot rule out that some are **F**, but overall it is clear that **AF** interactions dominate and lead to the small ground state spins determined experimentally.

CONCLUSIONS

The comproportionation reaction between Mn^{II} and Mn^{VII} in the presence of Ce(NO$_3$)$_3$ and excess RCO$_2$H at 150 °C has led to the synthesis of new Ce$_x$ MNPs of CeO$_2$ with a submonolayer of Mn$^{II/III}$ ions on the surface, providing molecular analogues of the CeO$_2$/MnO$_x$ composite oxides at high Ce:Mn ratios where the Mn atoms segregate on the surface of CeO$_2$ fluorite phases. In addition, the Ce$_6$, Ce$_{10}$, and Ce$_{19}$ cores of **1**−**3**, respectively, all have some point of novelty not seen previously for our homometallic ceria MNPs. (i) The Ce$_6$ octahedron of **1** has a rare μ_6-O^{2-} at its center. (ii) The edge-sharing Ce$_{10}$ bioctahedron is again seen in Ce/Mn chemistry even though it is unknown in homometallic Ce/O chemistry, our previous Ce$_{10}$ compound having a single Ce$_6$ octahedron with four additional Ce ions forming a concentric tetrahedron about it and thus an overall Ce$_{10}$ supertetrahedron topology. (iii) The beautiful Ce$_{19}$ octahedron of the cation of **3** is again unprecedented.

The submonolayer of Mn occurs as multiple discrete Mn$_x$ units, and there are four Mn$_5$ units and four additional Ce ions on the Ce$_{19}$ octahedron together making the {Ce$_{23}$Mn$_{20}$} cation of **3** the highest-nuclearity Ce/Mn cluster obtained to date. Its isolation opens up new avenues in Ce/Mn cluster chemistry, and further studies are in progress to extend this family to higher-nuclearity species and to other Ce:Mn ratios

that might have a complete monolayer or multilayer of surface Mn ions. In addition, the attainment of analogues with other d metals on the surface is currently under investigation.

ASSOCIATED CONTENT

ⓈⒾ Supporting Information

The Supporting Information is available free of charge at https://pubs.acs.org/doi/10.1021/acs.inorgchem.1c03719.

Ce, Mn, and O BVS tables and labeled structural figures (PDF)

Accession Codes

CCDC 2121875−2121877 contain the supplementary crystallographic data for this paper. These data can be obtained free of charge via www.ccdc.cam.ac.uk/data_request/cif, or by emailing data_request@ccdc.cam.ac.uk, or by contacting The Cambridge Crystallographic Data Centre, 12 Union Road, Cambridge CB2 1EZ, UK; fax: +44 1223 336033.

AUTHOR INFORMATION

Corresponding Author

George Christou − *Department of Chemistry, University of Florida, Gainesville, Florida 32611-7200, United States;* ⓞ orcid.org/0000-0001-5923-5523; Phone: +1-352-392-8314; Email: christou@chem.ufl.edu

Authors

Sayak Das Gupta − *Department of Chemistry, University of Florida, Gainesville, Florida 32611-7200, United States;* Present Address: S.D.G. and A.E.T.: Intel Corp., Hillsboro, OR 97124

Annaliese E. Thuijs − *Department of Chemistry, University of Florida, Gainesville, Florida 32611-7200, United States;* Present Address: S.D.G. and A.E.T.: Intel Corp., Hillsboro, OR 97124

Ethan G. Fisher − *Department of Chemistry, University of Florida, Gainesville, Florida 32611-7200, United States*

Khalil A. Abboud − *Department of Chemistry, University of Florida, Gainesville, Florida 32611-7200, United States*

Complete contact information is available at:
https://pubs.acs.org/10.1021/acs.inorgchem.1c03719

Notes

The authors declare no competing financial interest.

REFERENCES

(1) Mitchell, K. J.; Abboud, K. A.; Christou, G. Atomically-precise colloidal nanoparticles of cerium dioxide. *Nat. Commun.* **2017**, *8*, 1445.

(2) Thuijs, A. E.; Li, X.-G.; Wang, Y. P.; Abboud, K. A.; Zhang, X.-G.; Cheng, H.-P.; Christou, G. Molecular analogue of the perovskite repeating unit and evidence for direct MnIII-CeIV-MnIII exchange coupling pathway. *Nat. Commun.* **2017**, *8*, 500.

(3) Russell-Webster, B.; Abboud, K. A.; Christou, G. Molecular nanoparticles of cerium dioxide: structure-directing effect of halide ions. *Chem. Commun.* **2020**, *56*, 5382−5385.

(4) Mitchell, K. J.; Goodsell, J.; Russell-Webster, B.; Twahir, U.; Angerhofer, A.; Abboud, K. A.; Christou, G. Expansion of the Family

of Molecular Nanoparticles of Cerium Dioxide, and their Catalytic Scavenging of Hydroxyl Radicals. *Inorg. Chem.* **2021**, *60*, 1641−1653.

(5) Russell-Webster, B.; Lopez-Nieto, J.; Abboud, K. A.; Christou, G. Truly Monodisperse 'Molecular Nanoparticles' of Cerium Dioxide of 2.4 nm dimensions: A {Ce$_{100}$O$_{167}$} Cluster. *Angew. Chem., Int. Ed.* **2021**, *60*, 12591−12596.

(6) Cao, T. S.; Chen, D. T.; Abboud, K. A.; Zhang, X.; Cheng, H. P.; Christou, G. Feasibility of ground state spin switching in a molecular analogue of the mixed-metal oxides with the perovskite structure. *Polyhedron* **2020**, *176* (1−6), 114275.

(7) Tilley, R. J. D. *Perovskites: Structure−Property Relationships*; John Wiley and Sons, Ltd., 2016.

(8) Cheong, S. W.; Mostovoy, M. Multiferroics: a magnetic twist for ferroelectricity. *Nat. Mater.* **2007**, *6*, 13−20.

(9) Dong, S.; Liu, J. M. Recent progress of multiferroic perovskite manganites. *Mod. Phys. Lett. B* **2012**, *26* (1−26), 1230004.

(10) Salamon, M.; Jaime, M. The physics of manganites: structure and transport. *Rev. Mod. Phys.* **2001**, *73*, 583−628.

(11) Wang, Z.; Shen, G.; Li, J.; Liu, H.; Wang, Q.; Chen, Y. Catalytic removal of benzene over CeO$_2$−MnO$_x$ composite oxides prepared by hydrothermal method. *Appl. Catal. B Environ.* **2013**, *138−139*, 253−259.

(12) Wang, Z.; Deng, Y.; Shen, G.; Akram, S.; Han, N.; Chen, Y.; Wang, Q. Catalytic Degradation of Benzene over Nanocatalysts containing Cerium and Manganese. *Chemistry Open* **2016**, *5*, 495−504.

(13) Colman-Lerner, E.; Peluso, M. A.; Sambeth, J.; Thomas, H. Cerium, manganese and cerium/manganese ceramic monolithic catalysts. Study of VOCs and PM removal. *J. Rare Earths* **2016**, *34*, 675−682.

(14) Zhang, X.; Wei, J.; Yang, H.; Liu, X.; Liu, W.; Zhang, C.; Yang, Y. One-Pot Synthesis of Mn-Doped CeO$_2$ Nanospheres for CO Oxidation. *Eur. J. Inorg. Chem.* **2013**, *2013*, 4443−4449.

(15) Venkataswamy, P.; Jampaiah, D.; Lin, F.; Alxneit, I.; Reddy, B. M. Structural properties of alumina supported Ce−Mn solid solutions and their markedly enhanced catalytic activity for CO oxidation. *Appl. Surf. Sci.* **2015**, *349*, 299−309.

(16) Abecassis-Wolfovich, M.; Landau, M. V.; Brenner, A.; Herskowitz, M. Low-temperature combustion of 2,4,6-trichlorophenol in catalytic wet oxidation with nanocasted Mn−Ce-oxide catalyst. *J. Catal.* **2007**, *247*, 201−213.

(17) Chen, H.; Sayari, A.; Adnot, A.; Larachi, F. Composition−activity effects of Mn−Ce−O composites on phenol catalytic wet oxidation. *Appl. Catal. B Environ.* **2001**, *32*, 195−204.

(18) Imamura, S.; Doi, A.; Ishida, S. Wet Oxidation of Ammonia Catalyzed by Cerium-Based Composite Oxides. *Ind. Eng. Chem. Prod. Res. Dev.* **1985**, *24*, 75−80.

(19) Blanco, G.; Cauqui, M. A.; Delgado, J. J.; Galtayries, A.; Pérez-Omil, J. A.; Rodríguez-Izquierdo, J. M. Preparation and character-ization of Ce/Mn/O composites with applications in catalytic wet oxidation processes. *Surf. Interface Anal.* **2004**, *36*, 752−755.

(20) Kang, C. Y.; Kusaba, H.; Yahiro, H.; Sasaki, K.; Teraoka, Y. Preparation, characterization and electrical property of Mn-doped ceria-based oxides. *Solid State Ionics* **2006**, *177*, 1799−1802.

(21) Tang, X.; Li, Y.; Huang, X.; Xu, Y.; Zhu, H.; Wang, J.; Shen, W. MnO$_x$−CeO$_2$ mixed oxide catalysts for complete oxidation of formaldehyde: Effect of preparation method and calcination temper-ature. *Appl. Catal. B Environ.* **2006**, *62*, 265−273.

(22) Zhou, G.; Shah, P. R.; Gorte, R. J. A Study of Cerium−Manganese Mixed Oxides for Oxidation Catalysis. *Catal. Lett.* **2008**, *120*, 191−197.

(23) Wu, X.; Liu, S.; Weng, D.; Lin, F.; Ran, R. MnO$_x$−CeO$_2$−Al$_2$O$_3$ mixed oxides for soot oxidation: Activity and thermal stability. *J. Hazard. Mater.* **2011**, *187*, 283−290.

(24) Wu, L.; Dey, S.; Gong, M.; Liu, F.; Castro, R. H. R. Surface Segregation on Manganese Doped Ceria Nanoparticles and Relation-ship with Nanostability. *J. Phys. Chem. C* **2014**, *118*, 30187−30196.

(25) Lang, R.; Du, X.; Huang, Y.; Jiang, X.; Zhang, Q.; Guo, Y.; Liu, K.; Qiao, B.; Wang, A.; Zhang, T. Single-Atom Catalysts Based on the Metal−Oxide Interaction. *Chem. Rev.* **2020**, *120*, 11986−12043.

(26) Tasiopoulos, A. J.; Wernsdorfer, W.; Moulton, B.; Zaworotko, M. J.; Christou, G. Template Synthesis and Single-Molecule Magnetism Properties of a Complex with Spin *S* = 16 and a [Mn$_8$O$_8$]$^{8+}$ Saddle-Like Core. G. Christou. *J. Am. Chem. Soc.* **2003**, *125*, 15274−15275.

(27) Tasiopoulos, A. J.; O'Brien, T. A.; Abboud, K. A.; Christou, G. Mixed Transition Metal-Lanthanide Complexes at Higher Oxidation States: Heteronuclear Ce^{IV}- Mn^{IV} Clusters. *Angew. Chemie - Int. Ed.* **2004**, *43*, 345−349.

(28) Mishra, A.; Tasiopoulos, A. J.; Wernsdorfer, W.; Abboud, K. A.; Christou, G. High-Nuclearity Ce/Mn and Th/Mn Cluster Chemistry: Preparation of Complexes with [Ce$_4$Mn$_{10}$O$_{10}$(OMe)$_6$]$^{18+}$ and [Th$_6$Mn$_{10}$O$_{22}$(OH)$_2$]$^{18+}$ Cores. *Inorg. Chem.* **2007**, *46*, 3105−3115.

(29) Ma, C. B.; Hu, M. Q.; Chen, H.; Chen, C. N.; Liu, Q. T. A New Family of Homo- and Heterometallic Manganese Complexes at High Oxidation States Derived from the Oxidation of Mn^{II} with Ce^{IV}: Syntheses, Structures, and Magnetic Properties. *Eur. J. Inorg. Chem.* **2011**, *2011*, 5043−5053.

(30) Mereacre, V.; Ako, A. M.; Akhtar, M. N.; Lindemann, A.; Anson, C. E.; Powell, A. K. Homo- and Heterovalent Polynuclear Cerium and Cerium/Manganese Aggregates. *Helv. Chim. Acta* **2009**, *92*, 2507−2523.

(31) (a) Lampropoulos, C.; Thuijs, A. E.; Mitchell, K. J.; Abboud, K. A.; Christou, G. Manganese/Cerium Clusters Spanning a Range of Oxidation Levels and CeMn$_8$, Ce$_2$Mn$_4$, and Ce$_6$Mn$_4$ Nuclearities: Structural, Magnetic and EPR Properties. *Inorg. Chem.* **2014**, *53*, 6805−6816. (b) Papatriantafyllopoulou, C.; Abboud, K. A.; Christou, G. Mn/Ce Clusters from the use of pivalate and chelate ligands: Mn^{32II}$_8$Ce^{IV}, Mn^{III}$_2$Ce^{IV}$_2$, and Mn^{III}$_4$Ce^{III}$_2$ products. *Polyhedron* **2013**, *52*, 196−206.

(32) Maayan, G.; Christou, G. Old Clusters with New Function: Oxidation Catalysis by High Oxidation State Manganese and Cerium/Manganese Clusters Using O2 Gas. *Inorg. Chem.* **2011**, *50*, 7015−7021.

(33) Lan, T. X.; Zhang, X.; Chen, C. N.; Wang, H. S.; Wang, M.; Fan, Y. H. Synthesis and electrocatalytic reactivity for water oxidation of two cerium complexes. *J. Coord. Chem.* **2018**, *71*, 1415−1429.

(34) Malaestean, I. L.; Ellern, A.; Kögerler, P. {Ce$_{10}$Mn$_8$}: Cerium Analogues of the Decavanadate Archetype. *Eur. J. Inorg. Chem.* **2013**, *2013*, 1635−1638.

(35) Thuijs, A. E.; Marton, A.; Stamatatos, T. C.; Abboud, K. A.; Christou, G. High Nuclearity Cerium-Manganese Clusters and their Structural and Magnetic Properties: Ce^{IV}$_3$Mn^{III}$_7$ and Ce^{IV}$_5$Mn^{III}$_{11}$. *Polyhedron* **2016**, *103*, 288−294.

(36) Vincent, J. B.; Chang, H. R.; Folting, K.; Huffman, J. C.; Christou, G.; Hendrickson, D. N. Preparation and physical properties of trinuclear oxo-centered manganese complexes of general formulation [Mn$_3$O(O$_2$CR)$_6$L$_3$]$^{0,+}$ (R = Me or Ph; L = a neutral donor group), and the crystal structures of [Mn$_3$O(O$_2$CMe)$_6$(pyr)$_3$]-(pyr) and Mn$_3$O(O$_2$CPh)$_6$(pyr)$_2$(H$_2$O)]. *J. Am. Chem. Soc.* **1987**, *109*, 5703−5711.

(37) Sheldrick, G. M. Crystal structure refinement with SHELXL. *Acta Crystallogr., Sect. C: Struct. Chem.* **2015**, *71*, 3−8.

(38) Spek, A. L. PLATON SQUEEZE: a tool for the calculation of the disordered solvent contribution to the calculated structure factors. *Acta Crystallogr.* **2015**, *C71*, 9−18.

(39) Sheldrick, G. M. SHELXT-Integrated space-group and crystal-structure determination. *Acta Crystallogr., Sect. A* **2015**, *71*, 3−8.

(40) Chilton, N. F.; Anderson, R. P.; Turner, L. D.; Soncini, A.; Murray, K. S. PHI: A powerful new program for the analysis of anisotropic monomeric and exchange-coupled polynuclear *d*- and *f*-block complexes. *J. Comput. Chem.* **2013**, *34*, 1164−1175.

(41) (a) Brown, I. D.; Altermatt, D. Bond-valence parameters obtained from a systematic analysis of the Inorganic Crystal Structure Database. *Acta Crystallogr. Sect. B* **1985**, *41*, 244−247. (b) Brese, N.

E.; O'Keeffe, M. Bond-valence parameters for solids. *Acta Crystallogr. Sect. B* **1991**, *47*, 192−197.

(42) (a) Estes, S. L.; Antonio, M. R.; Soderholm, L. Tetravalent Ce in the Nitrate-Decorated Hexanuclear Cluster $[Ce_6(\mu_3\text{-}O)_4(\mu_3\text{-}OH)_4]^{12+}$: A Structural End Point for Ceria Nanoparticles. *J. Phys. Chem. C* **2016**, *120*, 5810−5818. (b) Hennig, C.; Ikeda-Ohno, A.; Kraus, W.; Weiss, S.; Pattison, P.; Emerich, H.; Abdala, P. M.; Scheinost, A. C. Crystal Structure and Solution Species of Ce(III) and Ce(IV) Formates: From Mononuclear to Hexanuclear Complexes. *Inorg. Chem.* **2013**, *52*, 11734−11743.

(43) (a) Das, R.; Sarma, R.; Baruah, J. B. A Hexanuclear Cerium(IV) Cluster with Mixed Coordination Environment. *Inorg. Chem. Commun.* **2010**, *13*, 793−795. (b) Mathey, L.; Paul, M.; Copéret, C.; Tsurugi, H.; Mashima, K. Cerium(IV) Hexanuclear Clusters from Cerium(III) Precursors: Molecular Models for Oxidative Growth of Ceria Nanoparticles. *Chem. - Eur. J.* **2015**, *21*, 13454−13461.

(44) (a) Hegetschweiler, K.; Schmalle, H. W.; Streit, H. M.; Gramlich, V.; Hund, H. U.; Erni, I. A simple, efficient route to a μ_6-oxo-centered hexanuclear iron(III) alkoxide complex: preparation and structure of $Na_2Fe_6O(OCH_3)_{18}\cdot6CH_3OH$. *Inorg. Chem.* **1992**, *31*, 1299−1302. (b) Botezat, O.; van Leusen, J.; Kögerler, P.; Baca, S. G. Tuning the condensation degree of $\{Fe^{III}n\}$ oxo clusters via ligand metathesis, temperature, and solvents. *Inorg. Chem.* **2018**, *57*, 7904−7913. (c) Grebenyuk, D.; Martynova, I.; Tsymbarenko, D. Self-Assembly of hexanuclear lanthanide carboxylate clusters of three architectures. *Eur. J. Inorg. Chem.* **2019**, *2019*, 3103−3111.

(45) Malaestean, I. L.; Ellern, A.; Baca, S.; Kögerler, P. Cerium oxide nanoclusters: commensurate with concepts of polyoxometalate chemistry? *Chem. Commun.* **2012**, *48*, 1499−1501.

(46) Russell-Webster, B.; Lopez-Nieto, J.; Abboud, K. A.; Christou, G. Phosphorus-based Ligand Effects on the Structure and Radical Scavenging Ability of Molecular Nanoparticles of CeO_2. *Dalton Trans.* **2021**, *50*, 15524−15532.

(47) Loschen, C.; Migani, A.; Bromley, S. T.; Illas, F.; Neyman, K. M. Density functional studies of model cerium oxide nanoparticles. *Phys. Chem. Chem. Phys.* **2008**, *10*, 5730−5738.

(48) Wang, Z. L.; Feng, X. Polyhedral Shapes of CeO_2 Nanoparticles. *J. Phys. Chem. B* **2003**, *107*, 13563−13566.

(49) Wasson, M. C.; Zhang, X.; Otake, K.; Rosen, A. S.; Alayoglu, S.; Krzyaniak, M. D.; Chen, Z.; Redfern, L. R.; Robison, L.; Son, F. A.; Chen, Y.; Islamoglu, T.; Notestein, J. M.; Snurr, R. Q.; Wasielewski, M. R.; Farha, O. K. Supramolecular Porous Assemblies of Atomically Precise Catalytically Active Cerium-Based Clusters. *Chem. Mater.* **2020**, *32* (19), 8522−8529.

(50) Colliard, I.; Nyman, M. $Ce(IV)_{70}$ Oxosulfate Rings, Frameworks, Supramolecular Assembly, and Redox Activity. *Angew. Chem., Int. Ed.* **2021**, *60* (13), 7308−7315.

(51) (a) Flytzani-Stephanopoulos, M. Nanostructured Cerium Oxide "Ecocatalysts. *MRS Bull.* **2001**, *26*, 885−889. (b) Trovarelli, A. Catalytic Properties of Ceria and CeO_2-Containing Materials. *Catal. Rev.* **1996**, *38*, 439−520.